

ORIGINAL RESEARCH

Litz wire loss performance and optimization for cryogenic windings

Charalampos D. Manolopoulos¹  | Matteo F. Iacchetti^{1,2}  | Alexander C. Smith¹ | Paul Miller³  | Mark Husband³

¹Department of Electrical & Electronic Engineering, The University of Manchester, Manchester, UK

²Dipartimento di Energia, Politecnico di Milano, Milan, Italy

³Rolls-Royce Plc, Derby, UK

Correspondence

Matteo F. Iacchetti, Department of Electrical & Electronic Engineering, The University of Manchester, Oxford Road, Manchester, M13 9PL, UK.
Email: matteo.iacchetti@manchester.ac.uk

Abstract

Litz wires operating in a cryogenic environment can potentially improve both the efficiency and power density of electrical machines and passive components. However, due to the low resistivity and high magnetic fields, eddy-current losses may become significant in cryogenically cooled windings, especially in airgap winding arrangements or in the case of significant slot leakage fields, unless the litz wire parameters are carefully chosen. A framework for litz wire loss performance optimization and experimental characterisation at cryogenic temperatures is provided. An optimum operating temperature for minimum loss is derived based on analytical expressions, which highlights the role of litz wire parameters, current density and external field. The proximity loss model, used to calculate the optimum operating temperature, is validated experimentally. Two test rigs with different magnetic cores were designed and built. Copper and aluminium litz wires with a strand diameter down to 0.1 mm were tested in a liquid nitrogen bath with a uniform harmonic external magnetic field up to 0.5 T peak and a frequency up to 1 kHz. Measurements show good agreement with the theoretical results and confirm that the proposed model can be confidently used during the preliminary design of cryogenic windings.

KEYWORDS

electric motors, loss measurement, machine windings

1 | INTRODUCTION

Litz wires are multi-filament wires composed of very fine, insulated and twisted conductors (strands). Traditionally, litz wire windings are used in medium and high-frequency inductors and transformers [1, 2] to reduce the skin effect and proximity losses due to the leakage fields. Litz wire technology has also been considered to replace the stranded coils in stator windings in electrical machines [3] with both slotted and air-cored layouts where litz wires are exposed to high magnetic fields. Applications of air-cored designs with airgap-winding litz wire include large synchronous turbo-generators [4], high speed permanent magnet motors [5] and hybrid-superconducting machines [6, 7].

The losses in a litz wire are generally divided into skin losses and proximity losses. Different definitions have been used in the literature for these terms. For example, in Ref. [8], each loss factor is divided into strand and bundle level, and the

proximity losses are further divided into internal and external proximity losses. A simple definition of the losses is used in Refs. [9, 10]. Analytical loss equations for round conductor windings are developed in Refs. [11, 12].

A significant increase in power density and efficiency of electric components may be achieved by cooling down to cryogenic temperatures [13, 14]. Reduced Joule losses are also expected in an electrical machine winding operating at cryogenic temperatures [15, 16], potentially allowing a step change in performance compared to ordinary machines [17].

This will fit very well in some applications, such as marine and aerospace electric propulsion, where the cryogenic cooling may be provided 'for free' in the form of cryogenic fuel (e.g. LNG/LH₂ [liquid natural gas/liquid hydrogen]), which can then use the electric losses to evaporate and feed the engine/fuel cells. Cryogenically cooled 'hyper-conducting' windings can be made of readily available materials like

This is an open access article under the terms of the Creative Commons Attribution-NonCommercial-NoDerivs License, which permits use and distribution in any medium, provided the original work is properly cited, the use is non-commercial and no modifications or adaptations are made.

© 2022 The Authors. *IET Electric Power Applications* published by John Wiley & Sons Ltd on behalf of The Institution of Engineering and Technology.

copper (Cu) and aluminium (Al), but compared with room-temperature windings, they are more sensitive to eddy current losses so careful attention to the strand size and the twist/bunching arrangements is needed. Unlike high temperature superconductors (HTS) windings, they do not suffer from quench, which makes cryogenically cooled Cu and Al windings, a viable alternative to HTS for AC armatures [18]. By way of example, temperatures around 77 K enable an Al resistivity reduction by almost 20 times compared to that at normal operating temperatures around 400 K. As a drawback, however, the low resistivity may increase the winding skin effect and proximity losses significantly. To achieve substantial reduction of winding total losses using a litz wire technology in a cryogenic environment, the strand size has to be chosen appropriately, particularly considering the frequency and the presence of external fields. Unfortunately, there is a lack of results in the literature to inform the selection of the best cryogenic temperature level and strand parameters for given operating frequency, current density and external field levels experienced in typical airgap windings and coil sides facing significant slot leakage. As a result, the loss reduction in litz wires in winding arrangements operating at cryogenic temperatures is not optimised [19].

This paper investigates the loss performance of different litz wires operating at cryogenic temperatures and provides critical information to facilitate the preliminary design of litz wires used in cryogenically cooled windings. The focus is mainly on high external magnetic fields experienced in airgap windings or as a consequence of significant stray/leakage fields and the frequency range is typical of high-speed power-dense electrical machines. The key objectives including the novel contributions are as follows:

1. Discuss the effect of cryogenic temperature on proximity losses due to high external fields highlighting opportunities for design optimization and the test challenges.
2. Derive the optimum operating temperature for a given litz-wire specification and operating conditions in order to achieve minimum loss density.
3. Propose a comprehensive design framework for cryogenic test rigs to measure proximity losses under high external fields, including detailed guidelines on core material selection and rig setup and performance evaluation.
4. Provide experimental validation of the loss calculation, based on two different test-rig prototypes operating at Liquid Nitrogen (LN₂) temperatures.

2 | THEORETICAL BACKGROUND AND MODELLING

Adopting an approach similar to that in Refs. [9, 10], the total losses in a litz wire are divided into three major categories:

- 1) P_{rms} , ‘rms losses’: These losses are calculated by multiplying the squared rms current with the dc resistance. These losses are independent of the operating frequency.

- 2) P_{skin} , ‘Skin losses’: These losses are defined as the sum of the loss caused by the skin effect and the proximity losses caused by the surrounding strands in the litz wire (internal proximity losses).
- 3) P_{prox} , ‘Proximity losses’: These are the proximity losses caused by external fields. The origin of those external fields could be other conductors, leakage and main field in cored and coreless electrical machines, etc.

Figure 1 shows the current distribution of an ideal litz wire with radial and azimuthal transposition considering three different scenarios. The litz wire operates in LN₂ and has 61 Cu strands with a strand diameter equal to the skin depth of 0.77 mm. For dc current excitation, the current density has a uniform distribution as shown in Figure 1a. Figure 1b shows the current distribution at 1 kHz where the skin and proximity effect disturb the uniform pattern. In Figure 1c, an additional external magnetic field is applied with the same frequency. Depending on the external field strength, the current density pattern of Figure 1b is completely altered, losing its polar symmetry.

For a litz wire composed of cylindrical strands with a linear magnetic material, superposition is valid and loss components can be calculated independently [11]. As a result, the total losses are the sum of each loss component

$$P_{\text{tot}} = P_{\text{rms}} + P_{\text{skin}} + P_{\text{prox}} \quad (1)$$

For a fine litz wire with strand diameter less than the skin depth, $2r_s \leq \delta$, the reaction field due to the eddy currents can be neglected. As a result, the simplified expressions derived in [20, 21] are used for P_{skin} and P_{prox} in Equation (1), respectively. With these assumptions, the expression of total losses P_{tot} in a litz wire with N strands is

$$P_{\text{tot}} = \frac{R_{\text{dc}} \hat{I}^2}{2} + \frac{R_{\text{dc}} \hat{I}^2}{2} \left(\frac{N(N-1)}{8} \left(\frac{r_s}{r_L} \right)^2 \left(\frac{r_s}{\delta} \right)^4 \right) + \frac{N}{8} \omega^2 (\mu \hat{H})^2 \sigma \pi r_s^4 (\text{W/m}) \quad (2)$$

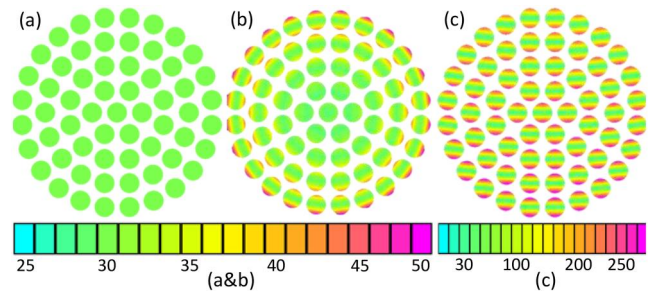


FIGURE 1 Current density distribution of an ideal copper litz wire carrying $14 A_{pk}$ in each strand. The current density colour scales are in A_{pk}/mm^2 . (a) dc, self-field; (b) 1 kHz, self-field; and (c) 1 kHz, 0.3 T external field.

with

$$R_{dc} = \frac{1}{N\sigma\pi r_s^2}, \delta = \sqrt{\frac{2}{\omega\mu\sigma}} \quad (3)$$

In Equations (2) and (3), \hat{I} is the peak of the sinusoidal current in the litz wire, \hat{H} is the peak of the sinusoidal external magnetic field strength, R_{dc} is the dc resistance of the litz wire per unit of length, δ is the skin depth, ω is the angular frequency, μ is the permeability, σ is the conductivity, and r_s and r_L are the radius of the strand and the litz wire, respectively.

Figure 2 illustrates the accuracy of (2) against the finite element (FE) results for the litz wire shown in Figure 1. Although the average current density was chosen equal to 30 A_{pk}/mm², proximity losses are the major loss contribution at strong external field levels.

3 | OPTIMUM TEMPERATURE FOR MINIMUM LOSSES

3.1 | Formulation

The power-loss density of a litz wire can be calculated by dividing Equation (2) with the total conductive area $N\pi r_s^2$ of the wire

$$P_{den} = \frac{\hat{J}^2}{2\sigma} + \frac{\hat{J}^2\sigma}{2} \left[\frac{N(N-1)}{32} \left(\frac{r_s}{r_L} \right)^2 r_s^4 \omega^2 \mu^2 \right] + \frac{1}{8} \omega^2 (\mu \hat{H})^2 r_s^2 \sigma \quad (\text{W/m}^3) \quad (4)$$

where $\hat{J} = \hat{I}/(N\pi r_s^2)$ is the average value (over the cross-sectional area) of the current density (peak) in a strand. From Equation (4), it is clear that a decrease in the operating temperature from room values to cryogenic levels will cause a drop in the rms loss and an increase of the skin and proximity

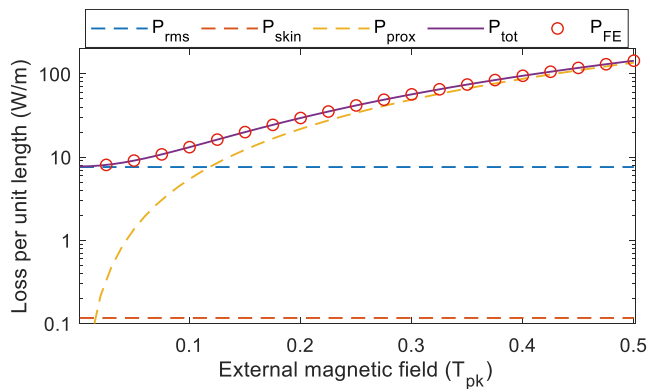


FIGURE 2 Comparison of analytical loss, P_{tot} (1), for the ideal litz wire shown in Fig. 1 with finite element (FE) results, P_{FE} , for strand diameter equal to skin depth ($2r_s = \delta$). The litz wire operates at 1 kHz at 77 K and the average current density is set to 30 A_{pk}/mm².

loss components. Considering normal litz wire parameters, the initial decrease of rms loss will be sharper than the increase of the other components, therefore resulting in a reduction of the overall power loss density. However, depending on the strand number, size and operating conditions, there is an ‘optimal’ temperature value at which the total loss density is minimised. Any further decrease in temperature below the optimal value will cause an increase in losses. The resistivity value at the optimal temperature is the ‘optimum resistivity’ and is obtained from the following optimality condition:

$$\frac{\partial P_{den}}{\partial \rho(T)} = 0 \quad (5)$$

where $\rho(T) = 1/\sigma(T)$ is the resistivity of the litz wire as a function of temperature. Solving Equation (5) gives the optimum resistivity as a function of litz wire parameters and operating conditions

$$\rho_{opt}(T) = \frac{\omega\mu r_s}{2} \sqrt{\frac{1}{8} N(N-1) \left(\frac{r_s}{r_L} \right)^2 r_s^2 + \left(\frac{\hat{H}}{\hat{J}} \right)^2} \quad (6)$$

For litz wires with a strand diameter less than the skin depth, $2r_s \leq \delta$ under a strong external magnetic field experienced in airgap windings, skin losses may be neglected. This approximation is acceptable for litz wires with a small number of strands. Although the error is higher for litz wires with a high number of strands, it drops to acceptable levels for high fields as shown in Figure 3. As a result, Equation (6) is simplified to

$$\rho_{opt}(T) = \frac{\omega\mu\hat{H}r_s}{2\hat{J}} \quad (7)$$

The litz wire-specific losses for optimum resistivity are

$$P_{den,opt} = \frac{1}{2} \hat{J} \omega \mu \hat{H} r_s \quad (8)$$

Optimum temperature T_{opt} is obtained from Equation (7) by inverting the non-linear equation $\rho_{opt} = \rho(T_{opt})$, where $\rho(T)$ is the experimental resistivity versus temperature of the litz wire material.

3.2 | Discussion

Although Al is cheaper and significantly lighter than Cu, it is not a common choice for litz wires because its resistivity at near room temperature is typically 55%–60% higher than in Cu. Figure 4 shows the trend of resistivity versus temperature for 99.999% pure Al and 99.996% pure Cu wire. The wire samples were measured in a cryostat within the temperature

range 21–270 K. The resulting analytic expressions for the resistivity curve fitting functions $\rho_{\text{Al}}(T)$ and $\rho_{\text{Cu}}(T)$ are given in Equation (16) in the Appendix. Figure 4 shows that, as the temperature decreases, the resistivity of Al falls more quickly than in Cu, and below around 77.9 K becomes lower than Cu resistivity. Thus, Al litz wire operating at cryogenic temperatures may be a viable solution for windings of electrical machines to combine high operating power density and efficiency levels.

Equation (8) reveals that the optimal loss density for given frequency, current density and external field levels is proportional to the strand diameter. However, for a specific strand diameter, limited by manufacturing feasibility and/or cost, the minimum loss Equation (8) requires litz wire operating at the optimal temperature where the conductor resistivity matches the optimal resistivity Equation (7). Therefore, despite $P_{\text{den,opt}}$ Equation (8) and ρ_{opt} Equation (7) being independent of the conductor material, this will set the required optimal operating temperature to achieve minimum losses. Figure 5a,b show the loss-density contour lines as a function of strand diameter and temperature for Al and Cu litz wires for 15 $A_{\text{rms}}/\text{mm}^2$ current density and under an external, uniform, sinusoidal magnetic field of amplitude $\hat{B} = 0.5$ T. These values may be sensible for airgap windings in electrical machines. The thick red line in Figure 5a,b represents the optimal diameter vs. temperature relationship.

Figure 5c,d show the loss density versus temperature for Al and Cu, respectively, and for 0.03 and 0.18 mm strand

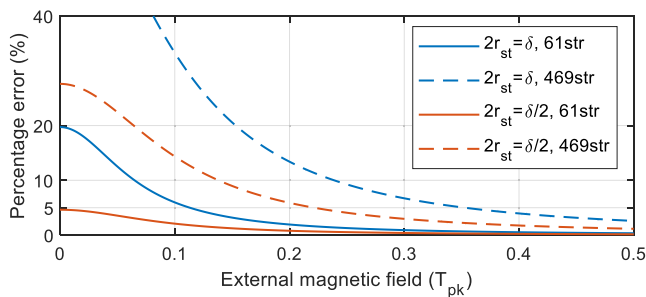


FIGURE 3 Loss error with external field for litz wire with different number of strands and strand diameters when neglecting the skin effect. The litz wires operate at 1 kHz at 77 K and the average current density is set to 30 $A_{\text{pk}}/\text{mm}^2$

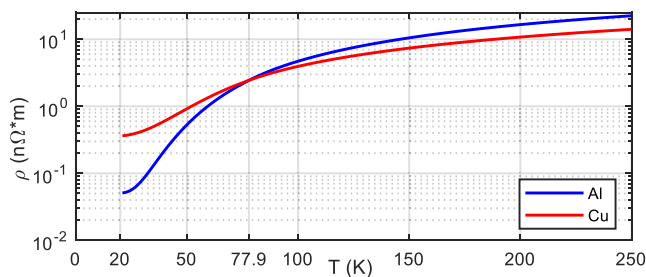


FIGURE 4 Resistivity of copper and aluminium at cryogenic temperatures.

diameters. These diameters may be deemed to be the minimum achievable values with two different technologies (or/and at two given costs). They yield optimal loss density values of 0.5 MW/m^3 and 3 MW/m^3 , respectively. The corresponding optimal temperature values for tested Al (Cu) grade are 61.2 and 117.7 K (54.7 and 139.7 K), respectively. For 0.18 mm, Al in the considered operating conditions, for instance, any further decrease in the operating temperature below 117.7 K would be detrimental. Furthermore, the density of the contour lines reveals that the sensitivity of the power loss density to the strand diameter is higher above the red line in Figure 5a,b. Thus, below the red line, a reduction of the strand diameter – should this be allowed by a new manufacturing technology – does not lead to significant gains in terms of loss density reduction.

Finally, the temperature of ≈ 77.9 K corresponds to the value at which the tested Al and Cu grades exhibit the same resistivity (see Figure 4). Therefore, regardless of the strand diameter, an Al litz wire operating between its optimal temperature and the critical value (e.g. within range 77.9–117.7 K for $2r_s = 0.18$ mm) outperforms Cu both in terms of weight and loss. The following points summarise the choice process between Al and Cu:

1. Find critical temperature, T_{cr} using the ρ versus T curves for the Cu and Al conductor materials.
2. Calculate optimal temperature for Al and Cu using (8) and ρ versus T curves for minimum strand diameter available (considering manufacturing and cost).
3. Calculate skin depth using (3) and check validity of $2r_s \leq \delta$
4. If the winding operating temperature is between T_{opt} for Al and T_{cr} , the Al conductor produces lower losses than copper and should be considered.

4 | TEST RIG DESIGN FOR PROXIMITY LOSS MODEL VALIDATION IN LIQUID NITROGEN

4.1 | Test-rig operation

Electrical machine airgap windings experience significant proximity loss due to high external fields. Proximity losses in litz wires have been measured for low magnetic fields (several mT) at high frequencies (10 kHz up to several MHz) and room temperature [9, 22].

The proposed test rig aims at measuring proximity losses at higher field values up to 0.5 T. The test rig is shown in Figures 6 and 7. Two C-cores facing each other and wound with ‘power coils’ form a small airgap that houses the Litz specimens Under Test (Litz Under Test (LUT)). By energising the power coils with AC current, a nearly uniform sinusoidal alternating magnetic field is created in the gaps, which links the LUT creating proximity losses. The LUT was placed at the centre of the airgap (Figure 6c) to ensure that all the strands of the LUT experienced a uniform external field. This was verified by hall sensor probe

measurements before the test (Section 4.3). The input power to the power coils is measured with and without LUT while monitoring the gap peak flux density via a hall sensor. As the LUT sample is not carrying any transport current, the difference of the two measurements is the proximity loss of the LUT.

4.2 | Design criteria

To obtain accurate measurements, the loss of the inductor should be kept comparable with the LUT loss. In other words, a high-accuracy test rig would have a high LUT to Test-rig *Loss Ratio* defined as

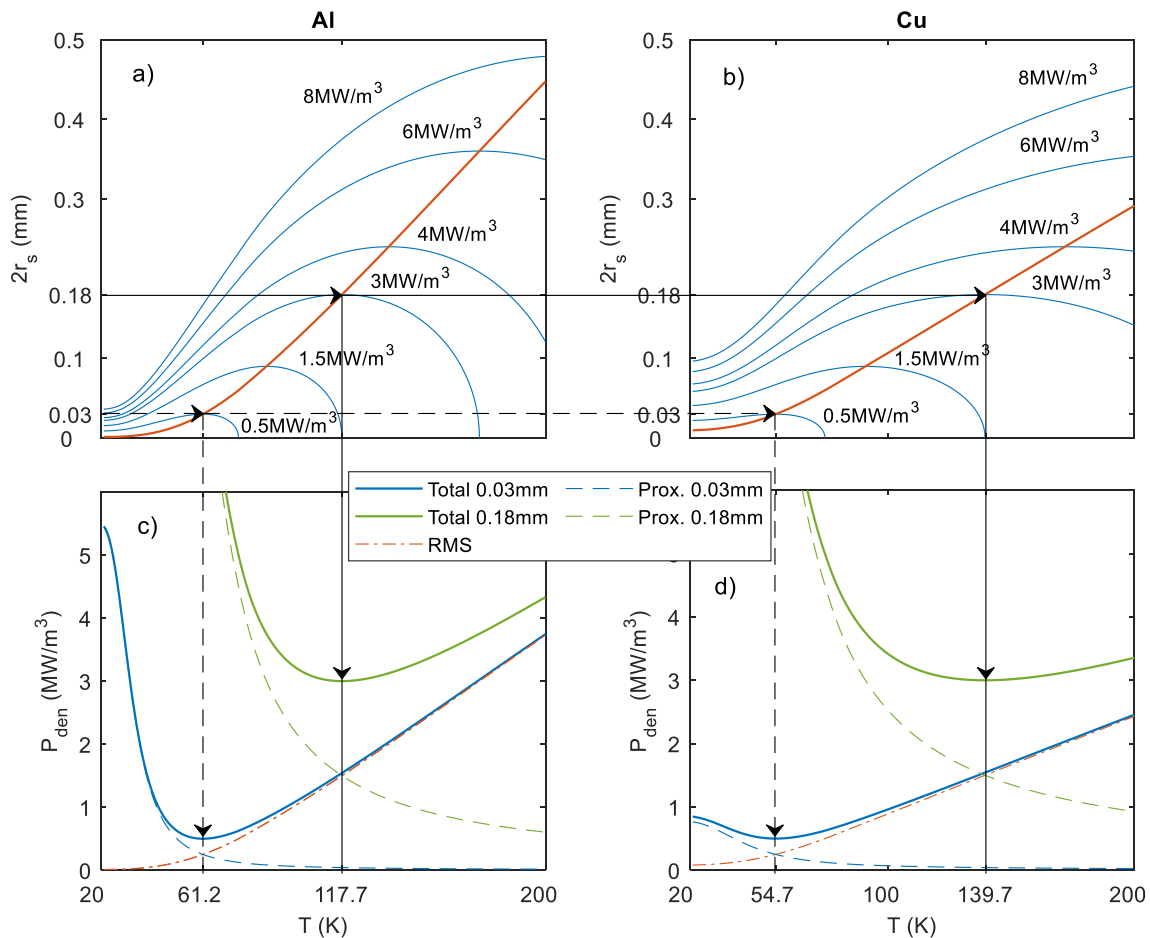


FIGURE 5 Loss-density characteristics for Al and Cu operating at 1 kHz, $J_{\text{rms}} = 15 \text{ A/mm}^2$ and $\hat{B} = 0.5 \text{ T}$. (a) and (b) Loss-density iso-lines as a function of T and r_s , for Al and Cu (blue lines), and optimal radius versus temperature (thick red lines). (c) and (d) Al and Cu loss-density versus-temperature profiles for diameters $2r_s = 0.03 \text{ mm}$ (blue lines) and $2r_s = 0.18 \text{ mm}$ (green lines).

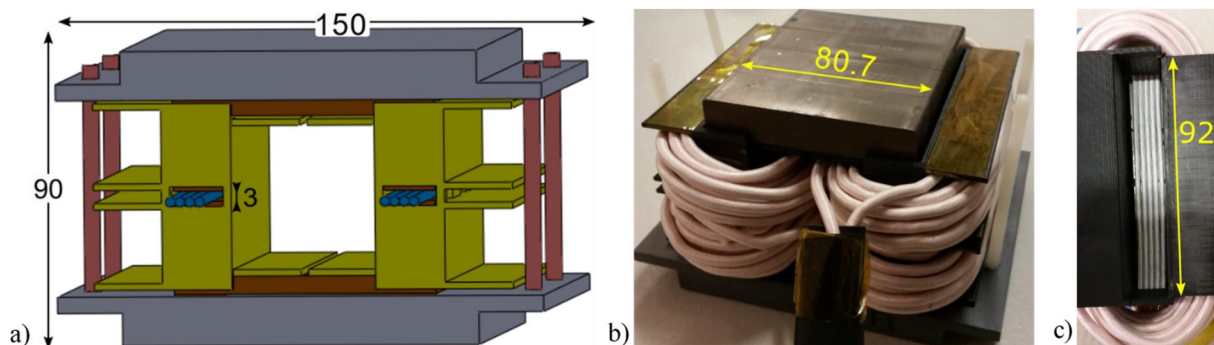


FIGURE 6 Design of the experimental rig without the power coil (a), test-rig assembly showing the cores below core holder top cap (b) and a side of the test rig showing the Litz Under Test (LUT) in the gap (c). All dimensions are in mm.

$$\text{Test - Rig Loss Ratio (TLR)} = \frac{P_1 - P_2}{P_1} 100\% \quad (9)$$

where P_1 and P_2 are the losses of the test rig with and without the LUT at the airgap, respectively.

For low-frequency applications, such as cryogenic electrical machines, the field should ideally have a high magnitude close to 1 T with frequencies up to 1 kHz. Therefore, the ideal core material should have high magnetic field saturation (>1.2 T), low losses for frequencies up to 1 kHz, and it should also maintain these desirable properties at cryogenic temperatures.

The proposed test rig consists of two arrays of U-cores facing each other. To maintain the LUT temperature at 77 K, the whole test rig was placed inside an LN₂ bath. The 2D FE model shown in Figure 7 was built to estimate the loss ratio (9) with different core materials, geometric and operating parameters and devise an optimised design. The litz wires used for the power coil and the LUT were modelled using a homogenised equivalent model to improve the simulation time [23]. Unfortunately, most of the datasheets for the core

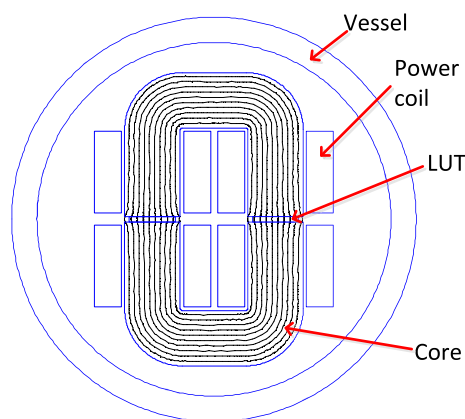


FIGURE 7 Test-rig cross-section used to test different core materials. The power coil has 25 turns of Cu litz wire with 1100×0.08 mm and 3.9 mm outer diameter.

materials focus on room-temperature properties only, so assumptions and extrapolations to cryogenic temperatures were made, where possible based on previous tests in the literature [24, 25]. Table 1 describes the magnetic materials considered for the core of the test rig.

Figure 8 shows the loss ratio Equation (9) for each material as a function of the field at the LUT. The LUT has 700 Al strands, 0.08 mm strand diameter, and an outer diameter of 3.2 mm. The gap is either 3.3 mm with one layer of litz wires or 6.5 mm with two layers. The selected frequency is 1 kHz. For low fields, ferrite is the obvious choice for the core because it gives the highest loss ratio. However, this ratio is likely to drop at 77 K because the performance of the ferrites deteriorates at low temperatures. The major disadvantage of ferrite is its low saturation field. That restricts the operation to field peak levels up to 0.35–0.36 T in order to avoid excessive magnetising current and losses in the power coil. The limit of 0.36 T was initially considered too low. Koolmu60, on the other hand, has a decent saturation level and the highest loss ratio after ferrite. Although Koolmu60 has half the relative permeability of

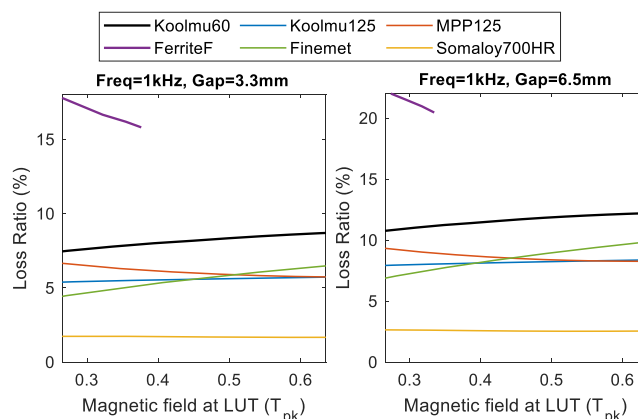


FIGURE 8 Loss ratio of the inductor shown in Figure 6 for different core materials versus the mean magnetic field at the Litz Under Test (LUT). The LUT has 700×0.08 mm strands with 9 wires (left) and 18 wires (right) in the gap.

TABLE 1 Magnetic materials considered for the core of the test rig

Core material	Composition	Available shapes	Bsat (T)	Performance at 77 K compared to room temperature ^a	
				Loss	Rel. perm/ty
Koolmu 60	Sendust powder	U-core, Toroid	1	Similar	Lower
Koolmu 125	Sendust powder	Toroid	1	Similar	Lower
MPP 125	Molypermalloy powder	Toroid	0.75	Similar	Similar
Ferrite F	Ferrite	U-core, Toroid	0.45	Higher	Lower
Somaloy700HR P	SMC	-	1.8	Higher	Similar
Finemet ^b	Nanocrystalline	U-core	1.2	-	-

Note: Somaloy is manufactured by Hognas, Finemet by Hitachi, and the rest by Magnetics.

Abbreviation: SMC, soft magnetic composites.

^aThe last two columns indicate the performance at 77 K based on [24, 25].

^bThis core is made by laminations so a building factor was used to include the 'gap losses' due to the fringing fields [26, 27].

Koolmu125, it gives a higher loss ratio, because in a gapped inductor, the equivalent relative permeability is determined mainly by the gap length. As a result, the Koolmu60 cores were chosen to build the first test rig able to operate with a maximum airgap peak field of 0.5 T.

Four cores per side were stacked together to achieve the preferred axial length. Two core holders and two bobbins were designed and manufactured to build the full assembly of the experimental rig shown in Figure 6. The power coil used Cu litz wire with an outer diameter of 4.1 mm comprising 1000 strands of 0.1 mm diameter. The strands have solder-strippable polyurethane film insulation Solderex/180. Strand insulation was tested successfully with a dc voltage up to 500 V in LN₂.

A second test rig was designed and built with the above criteria by using ferrite cores instead of Koolmu60 to achieve a higher loss ratio although the field was limited to 0.36 T. It was used for testing Cu litz wire with 0.1 mm strands, for which the first test rig would not give accurate results.

4.3 | Magnetic field and resistivity measurements

The magnetic field at the gap was measured using a search coil. The search coil was calibrated against three cryogenic hall sensors (HGCT 3020, Lakeshore) connected to a three-channel gaussmeter (Model 460, Lakeshore). The maximum frequency of the gaussmeter was 400 Hz, so a search coil was used to measure the magnetic fields up to 1 kHz. As shown in Figure 9, the gap spacer, built using a 3D printer, accommodates both the search coil and the three hall sensors in order to ensure they experience the same field during calibration.

The hall sensors were distributed along the gap length to check the uniformity of the magnetic field. The search-coil emf was filtered using a low-pass filter with a high cut-off frequency (>30 kHz) to ensure constant gain for frequencies below 1 kHz. The magnetic field, \hat{B} , can be calculated from the measured back-emf, \hat{E} , if the surface area, S , is known

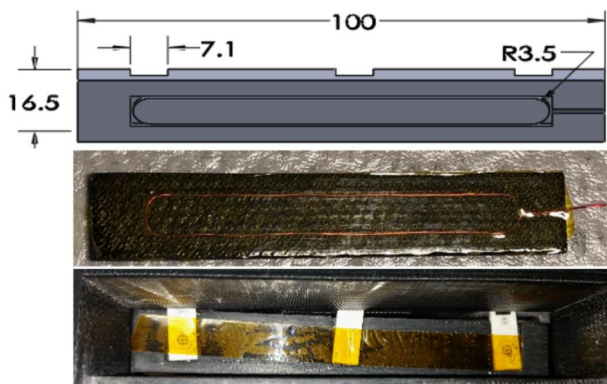


FIGURE 9 3 mm thick gap spacer design and dimensions in mm (top), search coil side (middle) and hall probes side (down) with the cryogenic hall probes

$$\hat{E} = \omega S \hat{B} \quad (10)$$

To avoid errors due to the calculation of S , the search coil was calibrated at 77 K using the hall sensors up to 400 Hz.

Figure 10 shows the results from the search coil calibration: the slope of the line is the effective cross-sectional area of the search coil. It was noticed that as the frequency increased, the measured field reduced but the emf divided by the frequency stays essentially constant. This was thought to be caused by the eddy currents induced in the hall sensor sheath, which opposed the main airgap field and reduced the measured value. As expected, higher currents in the power coil produce higher airgap field levels. The maximum field was obtained for 80 Arms in the power coil and is close to 0.5 Tpk.

As for the resistivity measurement, a single strand was carefully separated from the litz wire and tested in LN₂ with the four-probe method to measure the strand resistance accurately and then derive the resistivity. This procedure was applied to every tested litz wire sample to avoid errors in resistivity due to different purity of the conductor material.

4.4 | Loss measurement and power source

The most popular method for measuring the core loss is the ‘two winding technique’ where a primary (power) coil carries the excitation current and a secondary (search) coil provides an estimate of the back-emf across the magnetising branch [28, 29]. Another widely adopted electrical method uses an impedance analyser with or without a power amplifier to provide the excitation current [30]. The first method was impractical here because of the low-effective relative permeability of the gapped inductor. The high fringing fields do not allow the measured voltage of the secondary coil to be referred to the primary using simply the turns ratio. The second method was not applicable due to the small excitation current provided by the impedance analyser, which would limit the magnetic field in the airgap to be non-representative.

Due to these issues, a direct method was used to measure the losses of the experimental rig. The instantaneous current

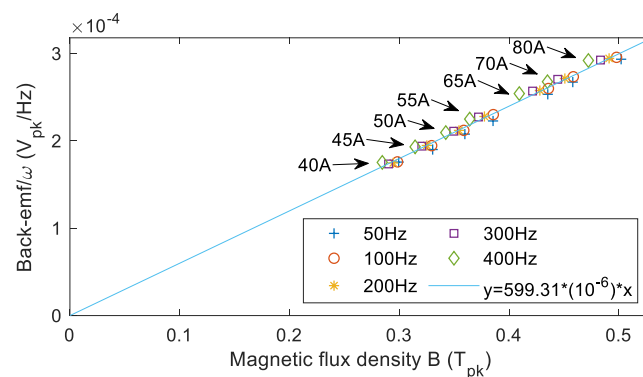


FIGURE 10 Search-coil back-emf divided by angular frequency versus magnetic field. The slope is the effective surface area of the search coil in LN₂

and voltage of the power coil were multiplied together to find the instantaneous power. The real power was calculated by averaging the instantaneous power over a number of cycles:

$$P = \frac{1}{T_{\text{span}}} \int_0^{T_{\text{span}}} u_{\text{pc}}(t) i_{\text{pc}}(t) dt \quad (11)$$

where u_{pc} is the voltage across the power coil, i_{pc} is the current of the power coil, and T_{span} is a multiple of the signal period. The voltage was measured through voltage taps soldered to the power coil litz wire ends. Figure 11 shows the schematic of the experimental apparatus. A 10 kVA, 300 V_{rms}, 80 A_{rms} single-phase linear power supply was used to energise the power coil. A 45 μF parallel capacitor bank provided reactive current compensation, allowing the test rig to be run up to 80 A within the power supply VA capability.

The test rig total losses are obviously dominated by the power coil and core losses, and in most tests, they were above 100 W, which caused severe boil-off of the LN₂. The LUT temperature was monitored with a thermocouple to make sure that no significant deviation from 77 K occurred during the tests and ensure consistency of the resistivity value used in Equations (3) and (4).

4.5 | Uncertainty analysis

Having established the loss measurement method, it is crucial to define a minimum *TLR* (*Test-rig Loss Ratio*) value allowing an acceptable uncertainty level, e_m , for the experimental litz loss measurement

$$\frac{\delta P_m}{P_m} \leq e_m \quad (12)$$

where $P_m = P_I - P_2$ is the litz loss measurement with P_1 and P_2 being the loss of the test rig with and without the LUT in the airgap, respectively. The numerator of (12) is

$$\delta P_m = e_p \sqrt{(P_1)^2 + (P_2)^2} \quad (13)$$

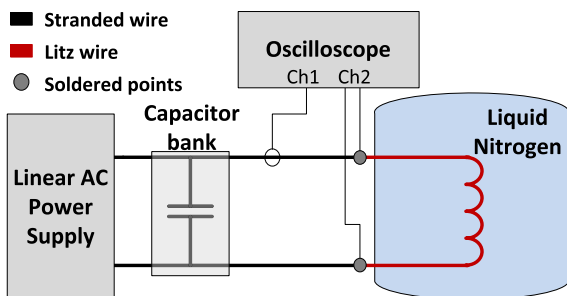


FIGURE 11 Loss measurement schematic.

where e_p is the power measurement uncertainty given by the uncertainty propagation analysis. Substituting Equation (13) into Equation (12) and $P_m = \text{TLR} \cdot P_1$ from Equation (9) yields

$$\frac{e_p \sqrt{(P_1)^2 + (P_2)^2}}{\text{TLR} \cdot P_1} \leq e_m \Rightarrow \frac{e_p}{e_m} \sqrt{1 + \left(\frac{P_2}{P_1}\right)^2} \leq \text{TLR} \quad (14)$$

Eliminating $P_2 = P_2 - P_1 + P_1 = (1 - \text{TLR}) P_1$ in (14) and solving for TLR gives

$$\text{TLR} \geq \frac{2(e_p/e_m)}{(e_p/e_m) + \sqrt{2 - (e_p/e_m)^2}} \quad (15)$$

Equation (15) is a key result as it sets the minimum TLR target for the test-rig design in order to meet the given measurement accuracy specifications.

In the measurement setup described earlier, the power measurement uncertainty was $e_p = 1.7\%$ and $e_p = 1.9\%$ for the first (koolmu) and second (ferrite) test rig, respectively, as shown in Figure 12. These were derived as a function of the power factor angle between voltage and current and considering probe uncertainties ($<1\%$) and residual delay time (20 ns) between the two channels after calibration with a deskew device. Despite the high power factor angle, the power measurement uncertainty remains low due to the low frequency (<1 kHz). By way of example, for an acceptable uncertainty $e_m = 15\%$ in the experimental litz loss measurement, the design target for the TLR from Equation (15) is 14.6% and 16.1% for the first and the second test rigs, respectively. Those values are within the estimated range from the sensitivity analysis carried out at the design stage using an FE analysis and this informed the selection of the cores.

5 | RESULTS

Table 2 collects the main data of the tested litz-wire samples along with the resistivity and the maximum peak field value in the testing conditions. Only ideal litz wires were considered,

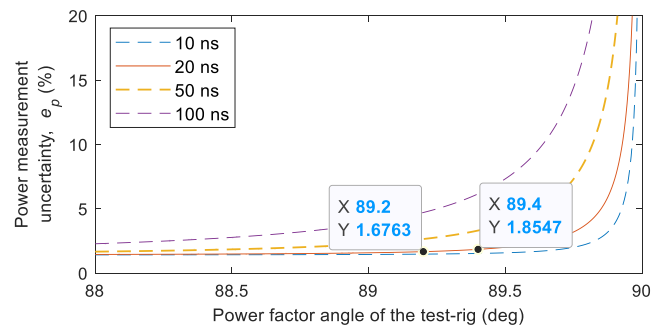










FIGURE 12 Power measurement uncertainty versus the power factor angle for 1 kHz. A deskew device was used to assure that the residual time delay between voltage and current was less than 20 ns. The current and the voltage magnitude uncertainties are 1% as per datasheet.

TABLE 2 Data of tested litz wire samples

	Copper						Aluminium	
Tested samples								
Strands No x Diam. (mm)	510 × 0.1	200 × 0.15	100 × 0.2	45 × 0.31	20 × 0.375	15 × 0.5	390 × 0.1	35 × 0.315
Wires No (at the gap)	14	8	8	8	8	6	20	8
Pitch length (mm)	≈55	≈45	≈45	≈35	≈35	≈35	≈55	≈35
Resistivity at 77K (nΩ·m)	2.167	2.182	2.200	2.323	2.100	2.120	3.127	3.057
Test rig ^a	#2	#1	#1	#1	#1	#1	#2	#1
\hat{B}_{max} (T)	0.36	0.49	0.49	0.49	0.49	0.49	0.36	0.49

^aTest rig #1-Koolmu cores with 92 mm length, test rig #2-ferrite cores with 120 mm length.

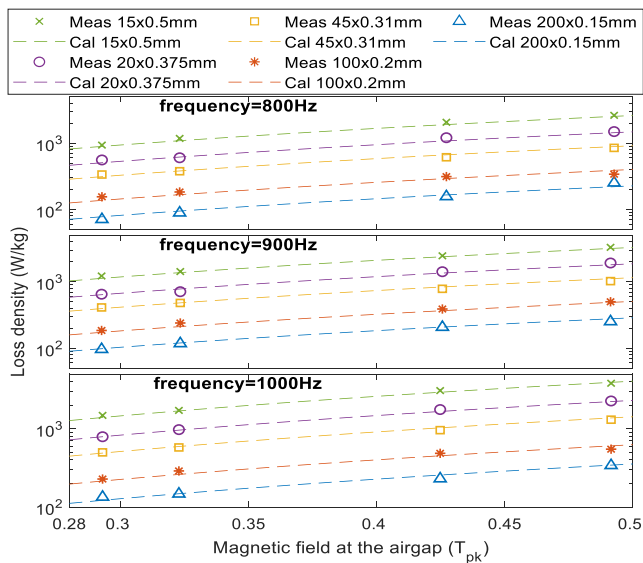


FIGURE 13 Measured and calculated, Equation (4), loss density versus external field at different frequencies, for Cu litz wire samples of different strand radii.

where the length exposed to the field is much bigger than the pitch length as these show an almost ideal behaviour [9]. Typical airgap windings usually have several pitches per coil. All the samples were tested at three frequencies: 800 Hz, 900 and 1000 Hz, as 1 kHz is the maximum frequency produced by the power supply. Four airgap field levels were tested in the test rig with Koolmu cores (test-rig #1): 0.29 T, 0.32 T, 0.42 T and 0.49 T. The corresponding rms current in the power coil was 40, 45, 65 and 80 A, where the last two values were achieved after adding the capacitor bank.

The difference between the rig input power with and without the LUT normalised to the LUT conductor volume

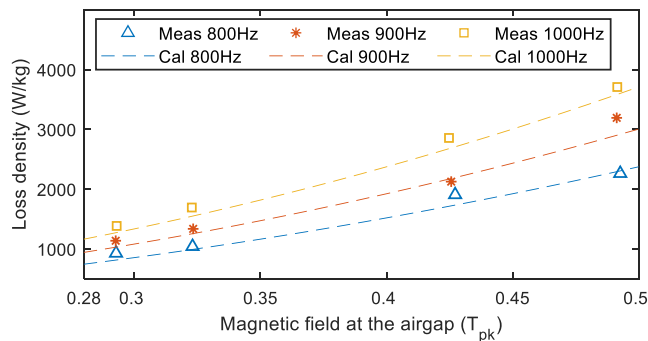


FIGURE 14 Measured and calculated, Equation (4), power density versus external field profiles at different frequencies, for the 35 × 0.315 mm Al litz wire.

was taken as a measurement of the LUT proximity loss density and compared with the theoretical predictions using Equation (4) for the measured field and resistivity. Figure 13 shows the LUT loss density versus the peak magnetic field obtained with the first test rig at different frequencies and with Cu LUT samples of different strand diameters. Al samples were tested as well and their proximity losses are shown in Figure 14. The discrepancy between theoretical and experimental values for the results shown in Figures 13 and 14 remains below 15%.

For litz wire samples with a strand diameter of 0.1 mm, proximity losses become very small, thereby reducing the loss ratio Equation (9) and hence accuracy. Therefore, the second test-rig ‘#2’ with ferrite cores instead of Koolmu was used, providing a higher loss ratio (see Figure 8) and better accuracy, albeit only allowing lower magnetic fields, up to 0.36 T. Also, the lower current in the power coil needed to achieve the maximum operating field of 0.36 T did not require the capacitor bank and allowed a power analyser to be used for

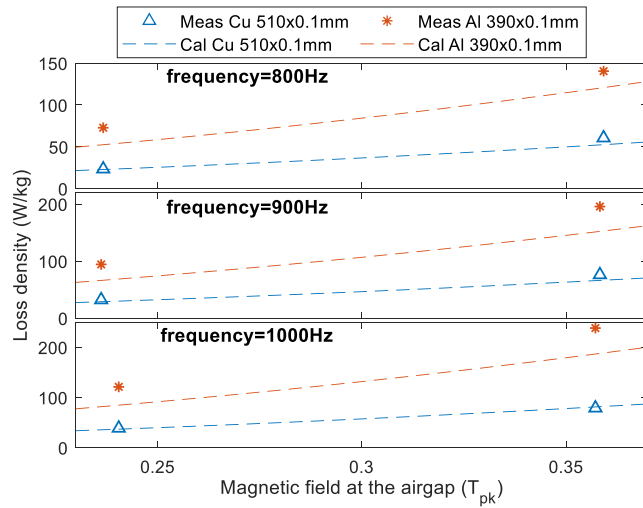


FIGURE 15 Measured and calculated, Equation (4), loss for 390×0.1 mm Al and 510×0.1 mm Cu litz wire measured with the ferrite-core test rig

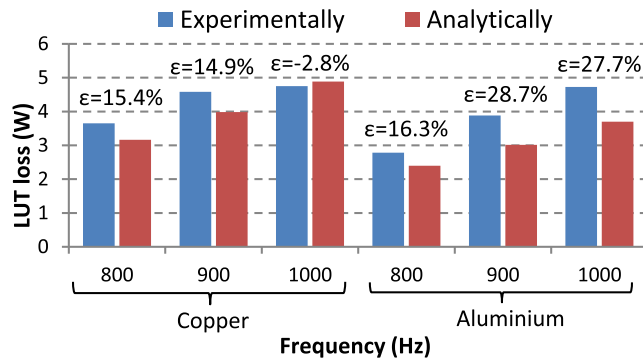


FIGURE 16 Comparison between measured and calculated loss for the 0.1 mm strand diameter copper and aluminium litz wire for $0.36 T_{pk}$ at the gap.

the measurements. The comparison between the experimental and theoretical results for 0.1 mm strand diameter Cu and Al litz wires is shown in Figure 15. For Cu, the experimental measurements follow the theoretical results, but the measured losses for Al remain higher than the corresponding theoretical values. The detailed loss values and errors between the theoretical and experimental results are given in Figure 16 for the high field measurements ($0.36 T_{pk}$). An error of less than 15.4% is observed with the second test rig for 0.1 mm strand diameter Cu litz wires. On the other hand, a higher discrepancy is observed for the 0.1 mm strand diameter Al litz wire. This is likely to be caused by the higher resistivity of the Al litz wire sample at 77 K as per Table 2 due to relatively low purity of Al. In fact, the experimental resistivity of 0.1 mm Al litz at 77 K is $3.127 \text{ n}\Omega\cdot\text{m}$ (see Table 2), that is, about 36% higher than that of tested Cu samples, therefore revealing a lower Al purity than what was initially envisaged. This causes a significant reduction in the TLR, which then produces a higher uncertainty e_m (by inverting Equation (15)) in the experimental results.

6 | CONCLUSION

This article investigates the loss performance of litz wires at cryogenic temperatures for low frequencies and under high external magnetic fields. These operating conditions are observed in air-cored armatures of emerging, power-dense, cryogenically cooled electrical machines and inductors/passives.

An expression for the optimum operating temperature for minimum loss has been derived combining ‘rms’, ‘skin’ and ‘proximity losses’.

Two new test rigs were designed and built to evaluate proximity losses of litz wires at LN_2 temperature independently of skin losses. The proximity loss model used in the optimization method was validated against measurements for peak fields up to 0.5 T and strand diameter down to 0.1 mm both for Cu and Al, showing good agreement. The maximum error was below 15.4%, apart from 0.1 mm Al wires (error slightly above 20%) where the testing conditions reach the accuracy limits of the test rig. As long as the skin depth remains higher than the strand diameter, the developed equations for the proximity loss, total loss density and optimum temperature allow extrapolation to thinner strands, higher field levels and different cryogenic temperature and provide a valuable tool for the optimal design of cryogenically cooled electrical components.

NOMENCLATURE

δ	skin depth (m)
μ	magnetic permeability (H/m)
ρ	electrical resistivity ($\Omega\cdot\text{m}$)
σ	electrical conductivity (S/m)
ω	angular frequency (rad/s)
\hat{B}	amplitude of magnetic field (T)
e_m, e_p	litz loss measurement, power measurement uncertainties
\hat{E}	amplitude of back-emf (V)
\hat{H}	amplitude of magnetic field strength (A/m)
\hat{I}	amplitude litz wire sinusoidal current (A)
$i_{pc}(t)$	instantaneous current of the power coil (A)
\hat{J}	amplitude of average current density in a strand (A/m ²)
LUT	litz wire Under Test
N	number of strands
P_1	loss of the test rig with the LUT at the airgap (W)
P_2	loss of the test rig without the LUT at the airgap (W)
P_{den}	total power loss density (W/m ³)
P_{FE}	finite element model power loss per unit length (W/m)
P_{prox}	proximity effect power loss per unit length (W/m)
P_{rms}	joule loss per unit length (W/m)
P_{skin}	skin effect power loss per unit length (W/m)
P_{tot}	total power loss in litz wire per unit length (W/m)
R_{dc}	dc resistance of the litz wire per unit of length (Ω/m)
r_L	litz wire radius (m)
r_s	single strand radius (m)
S	area of the search coil (m ²)
T	temperature (K)

TLR	test-rig loss ratio
T_{span}	multiple of the signal period (s)
$u_{\text{pc}}(t)$	instantaneous voltage of the power coil (V)

AUTHOR CONTRIBUTIONS

Charalampos D. Manolopoulos: Conceptualization; Formal analysis; Investigation; Methodology; Software; Validation; Visualization; Writing – original draft. **Matteo F. Iacchetti:** Conceptualization; Investigation; Methodology; Project administration; Supervision; Writing – review & editing. **Alexander C. Smith:** Conceptualization; Funding acquisition; Investigation; Methodology; Project administration; Supervision; Writing – review and editing. **Paul Miller:** Funding acquisition; Project administration; Supervision; Writing – review and editing. **Mark Husband:** Funding acquisition; Project administration; Supervision; Writing – review and editing.


CONFLICT OF INTEREST

The authors declare that there is no conflict of interest that could be perceived as prejudicing the impartiality of the research reported.

DATA AVAILABILITY STATEMENT

The data that support the findings of this study are available from the corresponding author upon reasonable request.

ORCID

Charalampos D. Manolopoulos  <https://orcid.org/0000-0002-5705-9068>

Matteo F. Iacchetti  <https://orcid.org/0000-0001-6961-4789>

Paul Miller  <https://orcid.org/0000-0003-0856-7194>

REFERENCES

- Patidar, B., et al.: Modelling and experimental demonstration of a litz coil-based high-temperature induction heating system for melting application. *IET Electr. Power Appl.* 12(2), 161–168 (2018). <https://doi.org/10.1049/iet-epa.2017.0256>
- Bie, Z., et al.: Current balance method of dual windings parallel coils based on distributed capacitor compensation in high-power Wpt systems. *IET Electr. Power Appl.* 16(2), 178–189 (2022). <https://doi.org/10.1049/elp.2.12145>
- Stipetic, S., Zarko, D., Kovacic, M.: Optimised design of permanent magnet assisted synchronous reluctance motor series using combined analytical–finite element analysis based approach. *IET Electr. Power Appl.* 10(5), 330–338 (2016). <https://doi.org/10.1049/iet-epa.2015.0245>
- Watanabe, M., et al.: Experimental-study of a practical airgap winding stator arrangement for large turbine generators. *IEEE Trans. Power Apparatus Syst.* 100(4), 1901–1910 (1981). <https://doi.org/10.1109/tpas.1981.316533>
- Lee, D., et al.: Optimisation method to maximise torque density of high-speed slotless permanent magnet synchronous machine in aerospace applications. *IET Electr. Power Appl.* 12(8), 1075–1081 (2018). <https://doi.org/10.1049/iet-epa.2017.0873>
- Wu, D., Chen, E.: Stator design for a 1000 Kw HTSC motor with air-gap winding. *IEEE Trans. Appl. Supercond.* 21(3), 1093–1096 (2011). <https://doi.org/10.1109/tasc.2010.2089962>
- Jansen, R., et al.: High efficiency megawatt motor conceptual design. In: 2018 Joint Propulsion Conference (2018)
- Sullivan, C.R.: 'Optimal choice for number of strands in a litz-wire transformer winding. *IEEE Trans. Power Electron.* 14(2), 283–291 (1999). <https://doi.org/10.1109/63.750181>
- Rossmannith, H., et al.: Measurement and characterization of high frequency losses in nonideal litz wires. *IEEE Trans. Power Electron.* 26(11), 3386–3394 (2011). <https://doi.org/10.1109/tpel.2011.2143729>
- Rosskopf, A., Bar, E., Joffe, C.: Influence of inner skin- and proximity effects on conduction in litz wires. *IEEE Trans. Power Electron.* 29(10), 5454–5461 (2014). <https://doi.org/10.1109/tpel.2013.2293847>
- Ferreira, J.A.: Improved analytical modeling of conductive losses in magnetic components. *IEEE Trans. Power Electron.* 9(1), 127–131 (1994). <https://doi.org/10.1109/63.285503>
- Tourkhani, F., Viarouge, P.: Accurate analytical model of winding losses in round litz wire windings. *IEEE Trans. Magn.* 37(1), 538–543 (2001). <https://doi.org/10.1109/20.914375>
- Haldar, P., et al.: Improving performance of cryogenic power electronics. *IEEE Trans. Appl. Supercond.* 15(2), 2370–2375 (2005). <https://doi.org/10.1109/tasc.2005.849668>
- Forsyth, A.J., et al.: Measurement and modelling of power electronic devices at cryogenic temperatures. *IEE Proc. Circ. Dev. Syst.* 153(5), 407–415 (2006). <https://doi.org/10.1049/ip-cds:20050359>
- Filusch, D., Breiteneder, M., Herzog, H.: Design of a hyperconducting synchronous machine for high-torque applications. In: XIII Int. Conf. Elect. Mach. (ICEM) (2018)
- Kim, H.M., et al.: Design of cryogenic induction motor submerged in liquefied natural gas. *IEEE Trans. Magn.* 54(3), 1–4 (2018). <https://doi.org/10.1109/tmag.2017.2751099>
- Zhang, X., et al.: Large electric machines for aircraft electric propulsion. *IET Electr. Power Appl.* 12(6), 767–779 (2018). <https://doi.org/10.1049/iet-epa.2017.0639>
- Sumption, M.D., et al.: Performance metrics of electrical conductors for aerospace cryogenic motors, generators, and transmission cables. *Cryogenics* 111, 103171 (2020). <https://doi.org/10.1016/j.cryogenics.2020.103171>
- Zheng, L., et al.: Design of a super-high speed permanent magnet synchronous motor for cryogenic applications. In: IEEE International Conference on Electric Machines and Drives (2005)
- Lotfi, A.W., Lee, F.C.: A high frequency model for litz wire for switch-mode magnetics. *Proc. IEEE Ind. Appl. Conf. 28th IAS Annu. Meeting, vol. 2* (1993)
- Acero, J., et al.: Simple resistance calculation in litz-wire planar windings for induction cooking appliances. *IEEE Trans. Magn.* 41(4), 1280–1288 (2005). <https://doi.org/10.1109/tmag.2005.844844>
- Tang, X., Sullivan, C.R.: Stranded wire with uninsulated strands as a low-cost alternative to litz wire. In: *Pesc'03: 2003 Ieee 34th Annual Power Electronics Specialists Conference*, 1–4, pp. 289–295. Conference Proceedings (2003)
- Meecker, D.: Continuum Representation of Wound Coils Via an Equivalent Foil Approach. <http://www.femm.info/examples/prox/notes.pdf> (2006). Accessed 18 Jun 2022
- Gerber, S.S., et al.: Performance of high-frequency high-flux magnetic cores at cryogenic temperatures. In: 2002 37th Intersociety Energy Conversion Engineering Conference (Iecec), pp. 249–254 (2002)
- Kapelski, D., et al.: The influence of the temperature of liquid nitrogen on the physical properties of powder magnetic composites. *Arch. Metall. Mater.* 60(2), 1323–1326 (2015). <https://doi.org/10.1515/amm-2015-0123>
- Odawara, S., et al.: Impact of material on the iron losses of a reactor with an air gap. *IEEE Trans. Magn.* 51(11), 1–4 (2015). <https://doi.org/10.1109/tmag.2015.2435012>
- Wang, Y., Calderon-Lopez, G., Forsyth, A.J.: High-frequency gap losses in nanocrystalline cores. *IEEE Trans. Power Electron.* 32(6), 4683–4690 (2017). <https://doi.org/10.1109/tpel.2016.2594083>
- Muhlethaler, J., et al.: Core losses under the dc bias condition based on steinmetz parameters. *IEEE Trans. Power Electron.* 27(2), 953–963 (2012). <https://doi.org/10.1109/tpel.2011.2160971>

29. Thottuvelil, V.J., Wilson, T.G., Owen, H.A.: High-frequency measurement techniques for magnetic cores. *IEEE Trans. Power Electron.* 5(1), 41–53 (1990). <https://doi.org/10.1109/63.45998>
30. Gradzki, P., Lee, F.C.: High-frequency core loss characterization technique based on impedance measurement. *HFPC proceedings* (1991)

How to cite this article: Manolopoulos, C.D., et al.: Litz wire loss performance and optimization for cryogenic windings. *IET Electr. Power Appl.* 17(4), 487–498 (2023). <https://doi.org/10.1049/elp2.12279>

APPENDIX

The general piecewise C^0 expression for Cu and Al resistivity in $n\Omega\cdot m$ in Figure 4 for T values within the range 21–270 K is

$$\rho(T) = \begin{cases} a_0 + a_1T + a_2T^2 + a_3T^3 + a_4T^4 & 20 \text{ K} \leq T \leq T_x \\ b_0 + b_1T + b_2T^2 + b_3T^3 + b_4T^4 & T_x \leq T \leq 270 \text{ K} \end{cases} \quad (16)$$

where coefficients a_i , b_i and T_x are given in Table A1.

Material	a_0 b_0 ($n\Omega\cdot m$)	a_1 b_1 ($n\Omega\cdot m/K$)	a_2 b_2 ($n\Omega\cdot m/K^2$)	a_3 b_3 ($n\Omega\cdot m/K^3$)	a_4 b_4 ($n\Omega\cdot m/K^4$)	T_x (K)
Cu	$3.692\cdot 10^{-1}$	$2.214\cdot 10^{-3}$	$-4.312\cdot 10^{-4}$	$1.679\cdot 10^{-5}$	$-9.311\cdot 10^{-8}$	75.4
	-2.484	$5.699\cdot 10^{-2}$	$1.078\cdot 10^{-4}$	$-3.917\cdot 10^{-7}$	$4.405\cdot 10^{-10}$	
Al	$-7.55\cdot 10^{-2}$	$2.167\cdot 10^{-2}$	$-1.283\cdot 10^{-3}$	$2.836\cdot 10^{-5}$	$-1.306\cdot 10^{-7}$	75.1
	-1.944	$1.958\cdot 10^{-3}$	$9.07\cdot 10^{-4}$	$-2.959\cdot 10^{-6}$	$3.447\cdot 10^{-9}$	

TABLE A1 Coefficients for the resistivity curve fit Equation (16) in Figure 4